Static and dynamic support of western United States topography

Thorsten W. Becker[a], Claudio Faccenna[b], Eugene D. Humphreys[c], Anthony R. Lowry[d], and Meghan S. Miller[a]

[a] Department of Earth Sciences, University of Southern California, MC 0740, 3651 Trousdale Pkwy, Los Angeles, CA 90089-0740, United States
[b] Dipartimento Scienze Geologiche, Università Roma TRE, Rome, Italy
[c] Department of Geological Sciences, University of Oregon, Eugene, United States
[d] Department of Geology, Utah State University, Logan, UT, United States

Highlights
• Isostatic models of topography improved using crustal structure from USArray passive seismology.
• Basin and Range shows anomalously high residual topography, Colorado Plateau appears normal.
• Mantle flow models predict most of the dynamic component of topography in western U.S.

Abstract
Isostatic and dynamic models of Earth's surface topography can provide important insights into the driving processes of tectonic deformation. We analyze these two estimates for the tectonically-active western United States using refined structural models derived from EarthScope USArray. For the crust, use of recent Moho depth measurements and crustal density anomalies inferred from passive source seismology improve isostatic models. However, seismically determined lithospheric thickness variations from "lithosphere/ asthenosphere boundary" (LAB) maps, and lithospheric and mantle density anomalies derived from heat flow or uppermost mantle tomography, do not improve isostatic models substantially. Perhaps this is a consequence of compositional heterogeneity, a mismatch between thermal and seismological LAB, and structural complexity caused by smaller-scale dynamics. The remaining, non-isostatic ("dynamic") component of topography is large. Topography anomalies include negative residuals likely due to active subduction of the Juan de Fuca plate, and perhaps remnants of formerly active convergence further south along the margin. Our finding of broad-scale, positive residual topography in the Basin and Range substantiates previous results, implying the presence of anomalous buoyancy there which we cannot fully explain. The Colorado Plateau does not appear dynamically anomalous at present, except at its edges. Many of the residual topography features are consistent with predictions from mantle flow computations. This suggests a convective origin, and important interactions between vigorous upper mantle convection and intraplate deformation.

Keywords
western United States; dynamic topography; mantle convection; Moho; LAB; EarthScope USArray

1. Introduction

The evaluation of crustal and lithospheric structure in light of seismological, gravity, and topography constraints can provide insights into the forces that drive tectonic deformation. One issue arising especially for continental plates is how much of the topographic signal is compensated by lateral variations in crustal and lithospheric thickness and densities (sometimes called the "static" component, even though lithospheric density variations may be of past convective origin), and how much is actively being supported by basal tractions due to mantle convection ("dynamic" in the sense of viscous stresses due to present-day convection leading to surface deflection) (e.g. Braun, 2010; Flament et al., 2013).

Such an analysis has a long history for distributed zones of tectonic deformation ("mobile belts") like the western United States (U.S.) (e.g. Crough and Thompson, 1977; Lachenbruch and Morgan, 1990; Jones et al., 1992; Jones et al., 1996; Lowry et al., 2000; Chase et al., 2002). Yet, many inferences, including the overall terminology, remain debated. For example, one may also use a broader definition of "mantle-driven dynamic topography" as that component of topography that has been modified within the last ~10 Ma by means of either active mantle tractions, or modified mantle lithospheric density (Karlstrom et al., 2012). Here, we proceed with the classic static vs. dynamic distinction in order to be able to conduct straightforward tests of isostatic compensation. However, we recognize the necessarily blurred nature of the dynamic processes at work within the thermo-chemical boundary layer of a convecting mantle, and will comment on some related issues in the discussion.

In general, most horizontal tectonic deformation in the western U.S. is related to Farallon plate subduction and hence a classic example of the link between plate system evolution and tectonics (Atwater, 1970). However, much of the region also appears to have experienced significant vertical forcing, across a range of spatial scales, and the relationship of such forcing to mantle dynamics remains to be fully quantified (e.g. Humphreys and Coblentz, 2007; Forte et al., 2010; Ghosh et al., 2013). Smaller-scale, upper mantle convection likely modulates the large-scale features and causes deformation within the actively deforming domain that extends from the Rocky Mountain front to the San Andreas Fault (Fig. 1a). Suggested connections range from shallow upper mantle processes, due to a flat slab subduction scenario (e.g. Spencer, 1996; Xue and Allen, 2007; Liu and Gurnis, 2010), perhaps via slab-plume interactions (Xue and Allen, 2007; Faccenna and Becker, 2010; James et al., 2011), to a link to deep mantle flow (e.g. Moucha et al., 2008; Forte et al., 2010). Within this context, it was suggested, for example, that a mantle upwelling may be the source of large-scale uplift in the Cordillera, perhaps associated with the Yellowstone plume (Crough and Thompson, 1977; Parsons et al., 1994). The Basin and Range region would then be expected to sit anomalously high compared to its crustal structure because it is atop a hot back-arc (Hyndman and Currie, 2011) and/or mantle plume supported (Lowry et al., 2000; Goes and van der Lee, 2002).
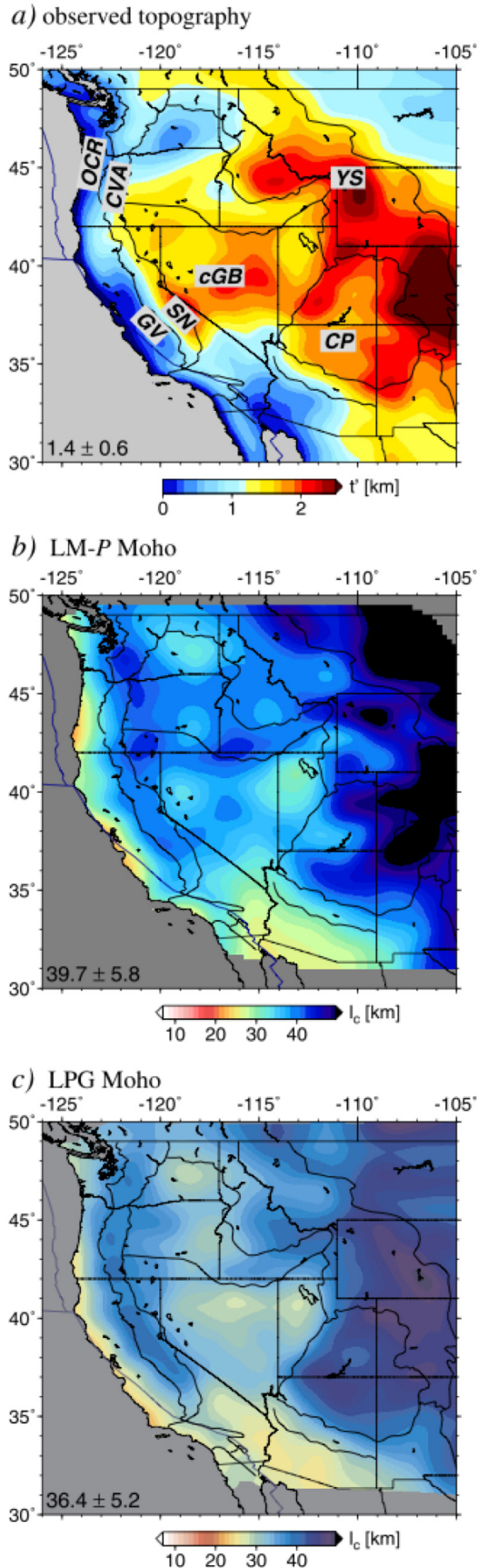
Fig. 1. (a) Long-wavelength filtered ETOPO2 (NOAA, 2006) topography (coloring, only showing positive topography, gray implying no available data in this and all subsequent plots). Dark blue lines are plate boundaries from Bird (2003). Geographic features: cGB, central Great Basin; CP, Colorado Plateau; CVA, Cascade Volcanic Arc; OCR, Oregon Coastal Ranges; SN, Sierra Nevada; YS, Yellowstone. Major morphological provinces shown with black lines. Legend inset in this and all subsequent maps indicates the mean and RMS variation of the property shown (units as in color scale). (b) Crustal thickness based on P receiver function estimates from Levander and Miller (2012), LM. (c) Crustal thickness from Lowry and Pérez-Gussinyé (2011), LPG.

Within the western Cordillera, the Colorado Plateau is another tectonic region of interest due to its apparent anomalous high topography, minimal deformation, thickened crust, and recent volcanism. There is growing consensus that volcanism and local uplift is pronounced around tectonic units such as the plateau itself (Parsons and McCarthy, 1995; Roy et al., 2009; Crow et al., 2010), perhaps because of small-scale convective or delamination processes (Bird, 1979; van Wijk et al., 2010; McQuarrie and Oskin, 2010; Levander et al., 2011). What is debated, however, is the large-scale dynamic support and the uplift history throughout the Cenozoic (e.g. Flowers, 2010; Karlstrom et al., 2012). One view holds that convective flow established dynamic support of the high topography fairly recently (Moucha et al., 2009; Karlstrom et al., 2012) including a present-day dynamic topography high underneath the plateau (Moucha et al., 2008). Others have shown that relatively steady, but positive dynamic topography might have been reached at ~40 Ma based on mantle flow (Liu and Gurnis, 2010), or thermal modeling in light of geological constraints and volcanism (Roy et al., 2009; Crow et al., 2010).

Structural models for the lithosphere that are well defined down to ~100 km scales are key for unraveling the issue of topographic support, and those have now been greatly facilitated in the

western U.S. by the advent of dense instrumentation such as EarthScope USArray (e.g. Lowry and Pérez-Gussinyé, 2011; Kumar et al., 2012; Levander and Miller, 2012; Shen et al., 2013). The resulting seismological constraints from passive imaging augment the patchwork of higher resolution, active source data (e.g. Mooney et al., 1998; Bassin et al., 2000) and regional broadband experiments (e.g. Karlstrom et al., 2012; Gilbert et al., 2012).

Here, we make use of these recent imaging advances and focus on a regional analysis, using receiver-function based crustal and lithospheric models on scales up to ~1500 km (Fig. 1), rather than a more local analysis (e.g. Parsons and McCarthy, 1995; Frassetto et al., 2006; Coblentz et al., 2011; Schulte-Pelkum et al., 2011; Bailey et al., 2012; Karlstrom et al., 2012). The latter can provide tighter bounds on the trade-offs, e.g. between layer thickness and density, and utilize local geological, and petrological constraints. The former is more readily compared with large-scale mantle-flow based estimates of topography, and can provide a backdrop upon which to improve with regional refinement.

Since it is a stress-based quantity, dynamic topography amplitudes from mantle flow scale, to first order, linearly with the density anomalies that cause mantle flow alone, unlike uplift rates, which go as density anomaly squared over mantle viscosity (e.g. Gurnis et al., 2000). Estimates of dynamic topography are predominantly sensitive to density structure in the upper ~400 km of the mantle for horizontal scales of ≤1000 km. Incorporating higher resolution tomographic constraints is therefore not merely an incremental advance, but the necessary requirement to analyze the potential link between tectonics and mantle dynamics at regional scales.

We first present a reanalysis of isostatic models for western U.S. topography using new structural models for the lithosphere, and then explore the degree to which the non-static component may be caused by mantle convection by means of global mantle circulation computations.

2. Methods and models

2.1. Isostatic balance

Our treatment of the "static" component of topography is standard but we briefly state the basics here for convenience (cf. Crough and Thompson, 1976; Bird, 1979). If a lithospheric column consisting of crustal layer thickness l_c and density ρ_c overlies a mantle lithosphere column of thickness l_l and density ρ_l, and floats freely within an asthenosphere of density ρ_a, the expected topography with respect to a reference level, e.g. a mid ocean ridge, is given by:

$$\hat{t} = f_1 l_c + f_2 l_l = f_3 l_c + f_2 L, \qquad (1)$$

where

$$f_1 = \frac{\rho_a - \rho_c}{\rho_a}, \quad f_2 = \frac{\rho_a - \rho_l}{\rho_a}, \quad f_3 = \frac{\rho_l - \rho_c}{\rho_a}, \qquad (2)$$

and $L = l_c + l_l$ is the total lithospheric thickness. The absolute predicted isostatic topography, t, is $t = \hat{t} + t_0$ (i.e. $t = t_0$ at $l_c = l_l = 0$); we use $t_0 = $ ~2.6 km for the mean ridge

level (Carlson and Johnson, 1994). Eq. (1) applies for land, but observed topography, t', with water coverage (i.e. bathymetry with $t' < 0$) of density ρ_w can be corrected by multiplying t' with $(\rho_a - \rho_w)/\rho_a$ before comparison with t. While seismological models are typically defined by spatially variable l_c based on inferred Moho depth and L based on lithospheric thickness proxies, writing the balance in terms of l_l as in the center of Eq. (1) is preferable because it disentangles ρ_c and ρ_l effects.

The relative importance of choices in the density values can be seen from Eq. (2). Here, we pick the average CRUST2.0 (Bassin et al., 2000) value for the domain under consideration, $\rho_c = 2836$ kg/m^3, as a reference and use a typical value of $\rho_l = 3250$ kg/m^3 as fixed (e.g. Lachenbruch and Morgan, 1990). We then find ρ_a from an L_1 norm minimization of the topography residual between predicted and actual topography

$$\delta t = t' - t, \text{ minimizing } M = \frac{1}{A}\int dA |\delta t|, \tag{3}$$

where A is the area under consideration. This procedure is not necessarily meant as an inversion for ρ_a but rather as a conservative "static" topography estimate, assigning the maximum possible topographic variations, within a simple model, to isostatic balance.

Fixing values to typical layer thicknesses of $l_c \sim 40$ km and $l_l \sim 36$ km (cf. Fig. 1 and Fig. 2), minimizing M yields $\rho_a = 3207$ kg/m^3. If, instead, we compute ρ_a from mean values (denoted by overbars), we find $\bar{\rho}_a = \left(\bar{l}_l \rho_l + \bar{l}_c \rho_c\right)/\left(\bar{l}_l + \bar{l}_c + t_0 - \bar{t}\right) = 3202$ kg/m^3. For the best-performing, spatially variable l_c models, $\rho_a \approx 3215$ kg/m^3, and such best-fit values are provided in all residual topography figures. With these choices, $f_1 \approx 0.12$ and $f_2 \approx -0.01$, i.e. crustal thickness variations are ~10 times more important for isostatic topography than lithospheric variations. Choosing different reference levels for t_0 will yield very similar results, with the main trade-off being with ρ_a. For $t_0 = -2.4$ km of Lachenbruch and Morgan (1990), our ρ_a estimates would be reduced by ~10 kg/m^3, for example. Similarly, ρ_a trades off with ρ_l in that the analysis is mainly sensitive to $\rho_l - \rho_a$.
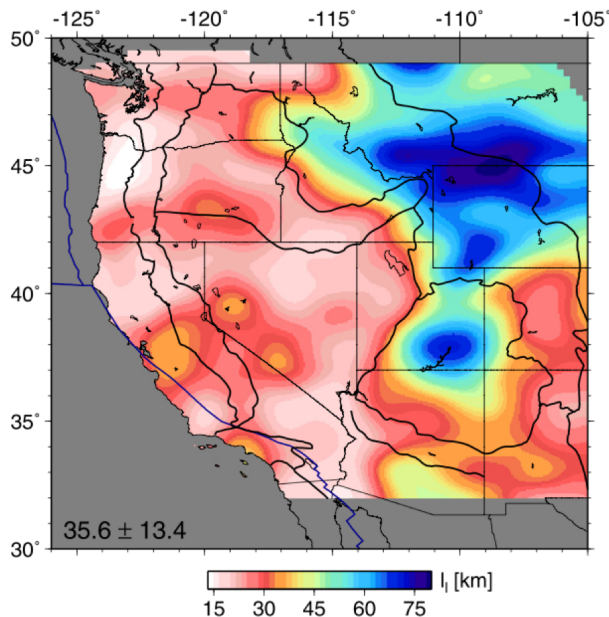

Fig. 2. Lithospheric mantle thickness, $l_l = L - l_c$, as inferred from the P-RF LAB depth from Levander and Miller (2012) and subtracting the corresponding P-RF Moho depth (Fig. 1b).

The residual topography, δt_c, after accounting for crustal thickness variations but using a fixed $\bar{l}_l$ for Eq. (1) may then be considered as either being caused entirely by mantle flow, or by means of lithospheric heterogeneity. Considering such heterogeneity, we can recast residual topography at constant ρ_a and ρ_l as being caused entirely by crustal density variations from a mean $\bar{\rho}_c$, assuming l_c and l_l fixed. In this case,

$$\Delta\rho_c = \rho_c - \bar{\rho}_c = -\rho_a \frac{\delta t_c}{l_c} \approx -80 \ \text{kg/m}^3 \cdot \delta t_l \ [\text{km}]. \tag{4}$$

Equivalently, for ρ_l variations at constant ρ_c,

$$\Delta\rho_l = -\rho_a \frac{\delta t_l}{l_l} \approx -89 \ \text{kg/m}^3 \cdot \delta t_l \ [\text{km}]. \tag{5}$$

Alternatively, assuming that ρ_c and l_c are constant, one may attribute all residual topography to variations of mantle lithospheric thickness,

$$\Delta l_l = l_l - \bar{l}_l = \frac{\delta t_c}{f_2} \approx -77 \cdot \delta t_c. \tag{6}$$

When we use a model with spatially variable mantle lithosphere thickness, we designate the corresponding residual topography anomalies as the lithospheric residual, δt_l, and minimize M for variable l_c and l_l. This typically leads to small differences of ρ_a from the value that would be estimated for constant $\bar{l}_l$.

2.2. Spatial filtering and correlation analysis

All spatial field input models were cut to the geographic region of interest, between 126°W–105°E longitude and 30°N–50°N latitude. We then performed a uniform, long-wavelength smoothing by convolution of these fields with a $6\sigma = 300$ km width Gaussian filter in order to minimize bias from short wavelength, flexural support and local heterogeneities. A Fourier analysis of radial power spectra indicates that such smoothing suppresses almost all power with wavelengths shorter than ~200 km. Given elastic thickness estimates for the western U.S. (Lowry and Pérez-Gussinyé, 2011), such smoothing should be sufficient to avoid flexural effects within most of the domain. There may be some remaining contamination within the stable continental interior toward the east, but we do not expect those features to affect our conclusions. Likewise, we explored different size smoothing kernels, and while mapped patterns and inferred density values are affected somewhat, our conclusions are robust with respect to this smoothing choice.

When comparing patterns between those long-wavelength smoothed fields, we typically consider a total, linear correlation coefficient, r ("correlation"), or r^2 (akin to a coherence), as computed from a ~10 km spaced, even area point sampling of the smoothed input grids. We will also discuss wavelength dependent correlation. Those are computed by first extrapolating all smoothed input fields to the full geographic domain considered, and then computing a range of bandpass-filtered realizations of those fields for a sliding center wavelength, λ. As bandpass, we use a 4th-order Butterworth filter on the Fourier coefficients with a range from 0.8λ to 1.2λ. All filtering operations were implemented using GMT (Wessel and Smith, 1998), version 4.5.7. Choices such as extrapolating, rather than using a smaller area, or the width of the bandpass, will affect results somewhat in an absolute sense, but relative model comparisons are meaningful. For the region under consideration, power estimates and correlations are then best constrained for wavelengths $\lambda \leq 1500$ km.

2.3. Structural models for the lithosphere

For topography, we use the ETOPO2 (NOAA, 2006) digital elevation model, only considering topography above sea level (Fig. 1a). We tested a range of seismologically defined models for crust and lithospheric structure. However, for the crust we focus on Ps receiver function (P-RF) thickness estimates from Levander and Miller (2012) (LM, Fig. 1b) and Lowry and Pérez-Gussinyé (2011) (LPG, Fig. 1c). Both estimates rely on the relatively dense coverage that USArray provides and were derived with comparable approaches, though methodological choices such as CCP stacking for LM, and likelihood filtering of automated Moho estimates (Crotwell and Owens, 2005) for LPG, differ. While the detailed implications of Moho structure have been discussed elsewhere (e.g., Karlstrom et al., 2012; Levander and Miller, 2012; Gilbert et al., 2012), we note a few features here. The large-scale patterns of Fig. 1 indicate that high topography in many regions such as the Colorado Plateau, the Rocky Mountains, and the Sierra Nevada are reflected in greater crustal thickness, as expected from a fully Airy-compensated crustal column, and this is not the case for much of the Basin and Range and the track of the Yellowstone hotspot (Lowry et al., 2000).

Overall, LM crustal thickness is slightly larger than for LPG (mean ± RMS ≈ 40±6 vs. 36±5 km). Such differences might be expected, e.g. given the trade-off between interface depth and velocity. Yet, overall crustal layer thickness patterns agree well; the total correlation between LM and LPG is $r = 0.88$.

The continental Moho is more complicated than the oceanic Moho. However, to a first approximation, the geophysically defined crust–mantle boundary, the depth where v_P jumps above 7.6 km/s, can be associated with a change in composition. Therefore, we assume that the major, shallow impedance contrast imaged by receiver functions at depth ranges between ~20 km and ~50 km in the western U.S. can be attributed to the contrast between crustal and mantle rocks. The deeper, negative velocity contrasts that are seen in receiver function or surface wave analysis at ~80 km may indicate a "lithosphere–asthenosphere boundary" (LAB), whose origin is, however, not entirely clear. The existence of a seismic LAB with sharp velocity decrease with depth is established beneath continental plates (e.g., Rychert and Shearer, 2009; Yuan and Romanowicz, 2010; Kumar et al., 2012) and may be associated with partial melt, a phase transition, changes in hydration state, and an increase in seismic anisotropy, or combinations thereof (Eaton et al., 2009; Fischer et al., 2010).

Detailed LAB maps are now available for the western U.S. (Kumar et al., 2012; Levander and Miller, 2012), but there are significant differences between lithospheric thickness from LAB depths and as would be inferred from interpreting the shallow, fast velocity anomalies of seismic tomography as indicative of a thermo-chemical boundary layer. Here, we will simply test if the LAB depths from Levander and Miller (2012) (P receiver function based as in Fig. 2) exert some control on the isostatic adjustment of a variable thickness, and constant density, lithosphere, assuming that a thermal boundary layer of variable thickness should approximately scale with the LAB. We will compare the resulting residual topography with that based on crustal thickness variations alone, and also evaluate lithospheric density anomalies at constant thickness from thermal models and uppermost mantle seismic tomography.

Fig. 2 shows one corresponding estimate for the lithospheric mantle thickness, $l_l = L - l_c$, using the Moho model of Fig. 1b. We recognize that LAB structure and interpretation is not straightforward, and Levander and Miller (2012) discuss lithospheric thickness variations based on both P and S (S-RF) receiver function analysis. In particular, the final LAB depths were provided by these authors merely as an estimate of a single, continuous surface throughout the entire western U.S., neglecting much of the complexity in the definition of the LAB and the signals themselves. P-RF and S-RF based LAB estimates from Levander and Miller are highly correlated ($r = 0.89$) with comparable means of $\bar{l}_l = 36\pm13$ vs. 43 ± 13 km, respectively. We note that the P-RF-based estimates for the LAB for the Rocky Mountains and the Colorado Plateau used the S-RFs as a guide due to the complexity of the signal, and we will only discuss the P-RF LAB subsequently.

With these caveats, it is apparent that the westernmost U.S. lithosphere is inferred to be relatively uniformly thin ($l_l \sim 26$ km vs. $\bar{l}_l \sim 36$ km), with the demarcation between small and large thickness following the Cordilleran hingeline and the western edge of the Colorado Plateau (Levander and Miller, 2012; Kumar et al., 2012). The regions east of the hingeline are inferred to not only have relatively large crustal, but also large mantle lithospheric thickness, except for the Rio Grande Rift. This is consistent with a relatively stronger lithosphere in those regions from effective elastic thickness estimates (Lowry and Pérez-Gussinyé, 2011).

By comparison of Fig. 1 and Fig. 2, it is clear that lithospheric thickness variations at constant ρ_l alone will not be a good predictor of topography for the western U.S. Relatively high-standing regions such as in the Colorado Plateau, the Rocky Mountains, the Rio Grande Rift Valley, and the Sierra Nevada would be expected to have relatively thin mantle lithosphere, while the opposite would be inferred from a simple interpretation of LAB depth. The total lithospheric layer thickness is $\bar{L} \approx 76$ km from P-RF and ≈ 80 km from S-RF (cf. Table 4 of Levander and Miller, 2012, for regional breakdown), roughly evenly distributed between crust and lithospheric mantle. L from seismological inferences on the LAB depth may be an underestimate of the actual, compositional thickness of the lithosphere. Given Eq. (1), our estimates of isostatic topography would then lead to a trade-off of l_l with f_2, i.e. an over-prediction of $\rho_l - \rho_a$.

2.4. Mantle flow modeling for convectively supported topography

We also provide estimates of the dynamic topography that would be expected from instantaneous mantle flow due to temperature anomalies in the mantle as inferred from seismic tomography (e.g., Le Stunff and Ricard, 1995; Panasyuk and Hager, 2000). Such studies have been conducted previously for the western U.S. using relatively low resolution, global tomographic models (Moucha et al., 2008; Liu and Gurnis, 2010; Forte et al., 2010). However, USArray has led to significantly improved upper mantle tomography for the western U.S. (e.g. Pavlis et al., 2012; Becker, 2012), partially motivating more recent dynamic topography computations (Ghosh et al., 2013).

We use two different flow modeling approaches. First, we infer dynamic topography from the radial tractions acting upon a free-slip surface boundary condition in an incompressible, Newtonian fluid spherical annulus that has only radial viscosity variations. These approximations allow for a semi-analytical solution of the mantle flow

problem based on a spherical harmonics expansion (Hager and O'Connell, 1981), and we expand the input density fields up to degree $\ell = 127$. This approach is comparable to the computations of Forte et al. (2010), for example. Our circulation model software (HC by Becker et al., 2013 and Steinberger, 2000) has been benchmarked and is available freely (e.g., Milner et al., 2009).

Given the scaling of dynamic topography, such simplified flow models provide a good first order estimate of the expected deflections given different density models, but the effects of appropriate plate motions and lateral viscosity variations may modulate the expression of spatial patterns. We therefore also pursue global finite element computations at uniformly high resolution of ~20 km, testing the response of crustal velocities and dynamic topography to prescribed Pacific plate motions (following Faccenna and Becker, 2010), or fully "dynamically-consistent" plate motions with prescribed weak zones (cf. Ricard and Vigny, 1989; Zhong et al., 2000), with model setup described in detail in Becker and Faccenna (2011).

In both approaches, we start from a deliberately simple, layered viscosity structure of $50\eta_0$, $0.1\eta_0$, η_0, $50\,\eta_0$ for the lithosphere (down to 100 km), asthenosphere (down to 410 km), transition zone viscosity η_0, and lower mantle (below 660 km), or similar. We also use a constant scaling between shear wave velocity and density anomalies such that $d\ln\rho/d\ln v_S \approx 0.2$ (Karato, 1993; Stixrude and Lithgow-Bertelloni, 2010), making the assumption that all anomalies are thermal, which will be discussed further below.

3. Results

3.1. Isostatic compensation

We first show isostatic balance computations for the "static" component of topography. Figs. 3a, b, and d show residual topography maps for constant crustal density. Given our minimization procedure for the misfit via Eq. (3), we can match the mean topography well, by design. However, the residual topography RMS, i.e. the deviation from a simple isostatic balance, is substantial; in fact, of the same order as the actual topography, ~0.6 km. Both crustal models predict broadly consistent patterns, with $r = 0.85$ correlation for LM and LPG Moho based estimates of residual topography as in Figs. 3a and b. This value is slightly different from the input model correlation as in Figs. 1b and c because of coverage and weighting. Values of $r \sim 0.8$ are typical for the crustal models we tested; LPG and LM δt_c correlate at $r = 0.89$ with model derived from Shen et al.'s (2013) Moho, for example.

The inferred residual topography shows broadly consistent features, perhaps associated with the Laramide orogeny and subsequent ignimbrite flareup, such as anomalously high topography in the Basin and Range (e.g., Parsons et al., 1994; Lowry et al., 2000). The Colorado Plateau and most of the Rocky Mountains are found to have relatively low-amplitude residual topography and are slightly lower than the mean isostatically predicted elevation. We also newly detect robust smaller-scale patterns on which we focus below. Many areas of young volcanic activity are anomalously high, for example, with the prominent exception of the Snake River Plain, where crustal intrusions of large volumes of dense gabbro have induced subsidence (e.g., McQuarrie and Rodgers, 1998).
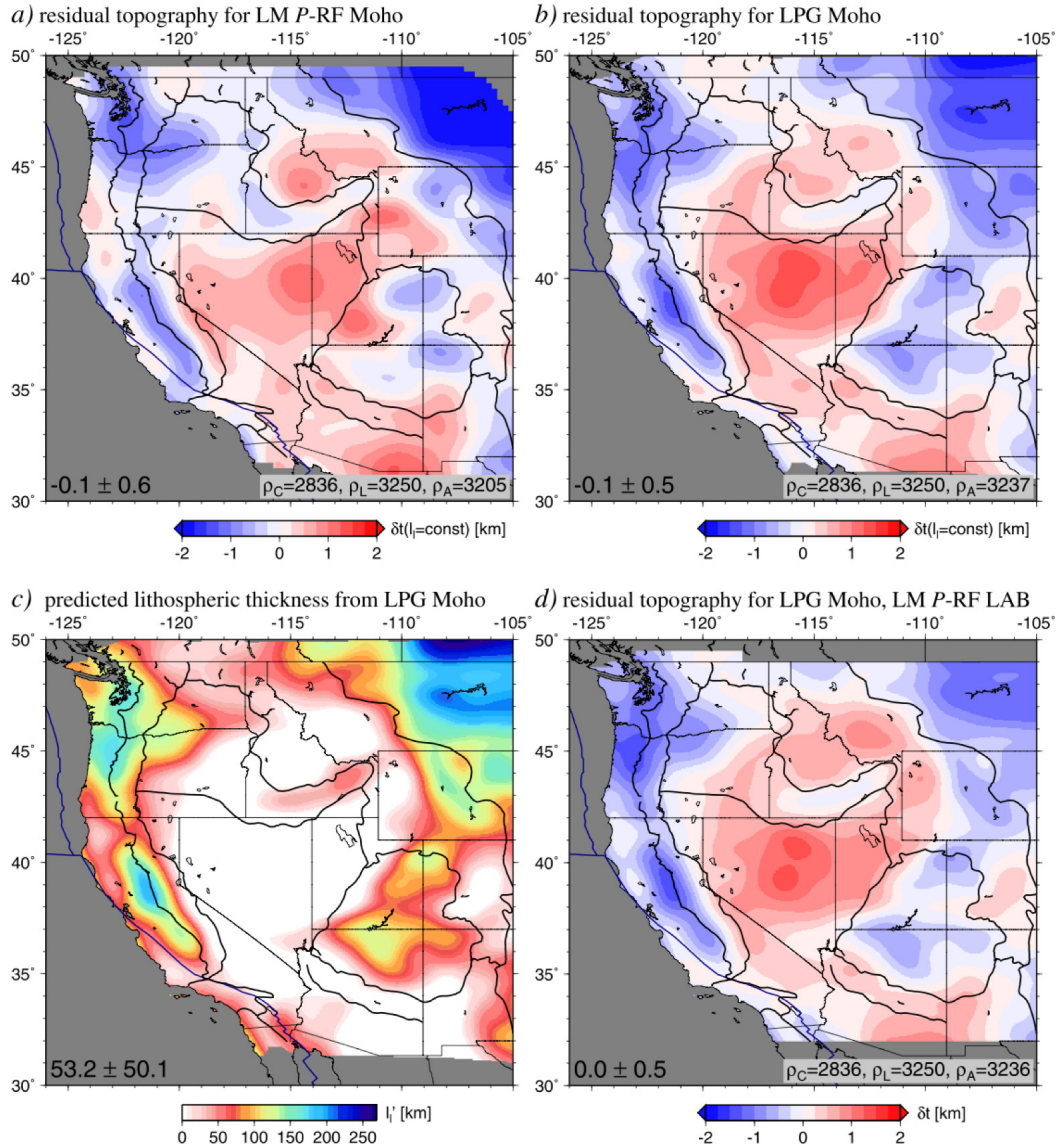
Fig. 3. (a) and (b): Residual topography, δt_c, for fixed lithospheric mantle thickness (set to the average from LM P-RF LAB) and crustal thickness from LM P-RF (a) and LPG (b) Mohos. (c) Predicted mantle lithospheric thickness at constant ρ_l if all residual topography inferred from (b) were due to lithospheric thickness variations. (d) Residual topography, δt_l, using the LPG crust and mantle lithosphere thickness from the LM P-RF LAB. ρ_c and ρ_l are assumed to be constant and ρ_a is found from minimizing M, with density values in kg/m^3 given in the figure legends. Correlation between predicted and observed topography is shown in Fig. 4 for (a), (b), and (d), and all subsequent residual topography maps.

We can also compare the wavelength-dependent coherence, as well as the spatial power, for predicted isostatic and observed topography (Figs. 4a and b). For constant crustal density and mantle lithospheric thickness, ~20…40% of the topography may be explained by crustal thickness variations, with a local maximum in correlation at $\lambda \sim 600$ km. Corresponding topography patterns at this wavelength are mainly a chain of high topography along the Sierra Nevada and Cascades, and local topography highs in the southern Colorado Plateau. Radial power spectra of inferred and actual topography are

similar up to ~1000 km wavelength. Applying the LPG crustal thickness estimates leads to a slightly better match than using LM-P, as also reflected in reduced RMS of the residual topography.
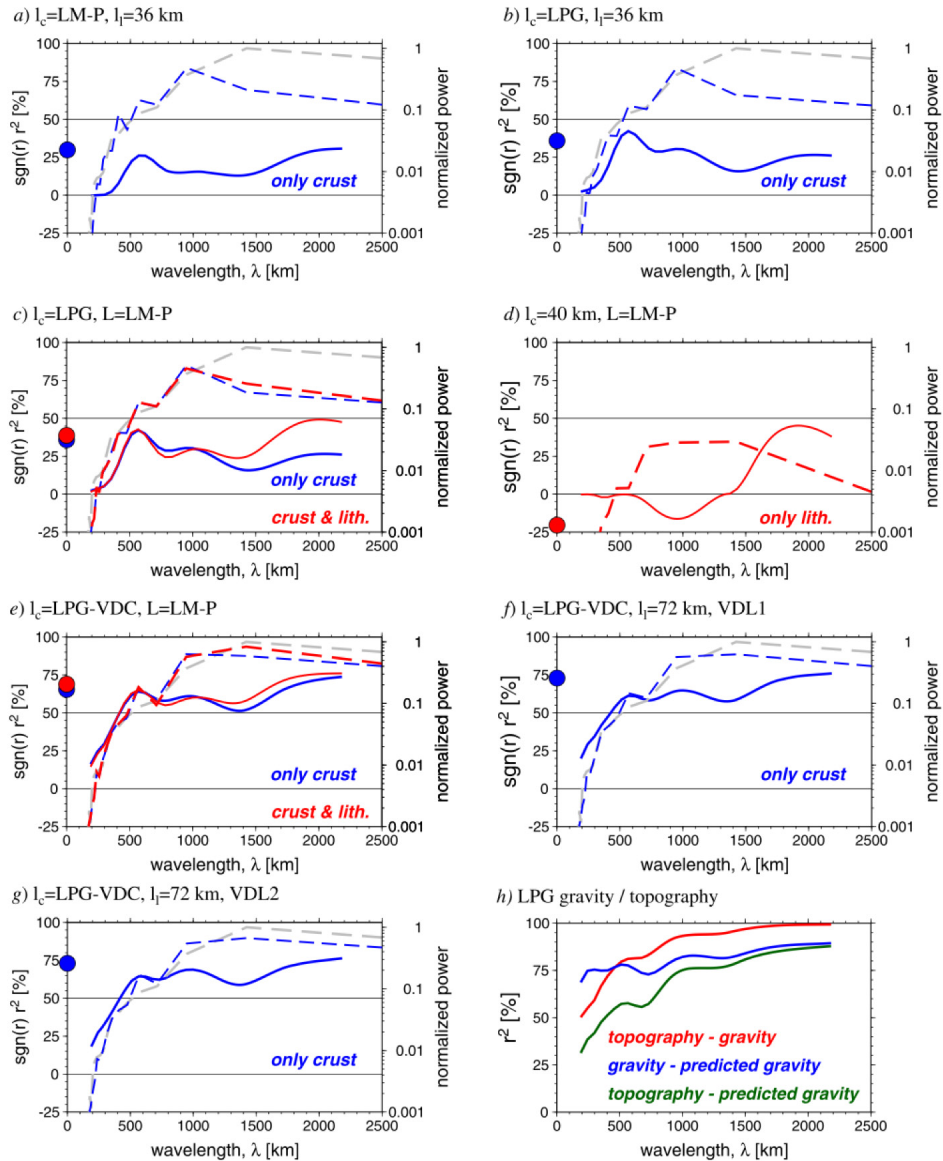

Fig. 4. (a)–(g): Wavelength-dependent signed correlation squared ($\text{sgn}(r)r^2$) between predicted isostatic and actual topography (solid) and normalized power spectra (dashed lines) for different crustal and lithospheric models. Blue and red curves are for constant and variable mantle lithospheric thickness, respectively. Power is normalized by the maximum in observed topography (gray line). Circles at zero wavelength denote the corresponding full field coherence. Sub-plot titles are for crustal, l_c, and lithospheric, l_l, models; if a specific value is given, those layers have constant thickness. (a) and (b) are the models from Figs. 3a and b using LM-P and LPG Moho, respectively; (c) adds lithospheric thickness variations from LM-P (Fig. 3d); (d) is an estimate of topography from lithospheric thickness variations alone; and (e) introduces crustal density variations to (c) (Fig. 5c). Plots (f) and (g) are for lithospheric density anomalies at exaggerated mantle lithospheric thickness of $l_l = 72$ km using tomography (Fig. 6a) and heat flow (Fig. 6b), respectively. Plot (h) shows the coherence (r^2) between topography, observed Bouguer gravity, and predicted gravity from LPG, all long-wavelength smoothed.

The addition of variations in lithospheric mantle thickness as inferred from LAB estimates does not lead to a marked reduction in residual topography RMS (Fig. 3d), and coherence is likewise only slightly improved (Fig. 4c). To explore the role of an LAB-based lithospheric correction further, Fig. 4d shows the topography coherence allowing for lithospheric thickness variations only, at constant crustal layer thickness. Such a model has overall negative correlation with topography, as expected given the inferences from crustal and lithospheric seismological models above. Only at the longest wavelengths of ~2000 km, where our correlation and power estimates are biased by the domain boundary, does such a purely lithospheric thickness model lead to relatively good topography pattern predictions. This maximum corresponds to a broad match of NW-SE oriented high topography along the Cordillera, as opposed to the more stable eastern U.S., barely imaged by the receiver function studies. The improvements in correlation of the variable lithosphere model in Fig. 4c compared to Fig. 4b may then be explained by this broad Cordillera shift, but the residual topography signal itself is small because of the density ratios $f_1 \gg f_2$.

Put differently, were all residual topography in the crustal model of Fig. 3b caused by mantle lithospheric thickness, l_l, variations, Eq. (6) predicts RMS variations in l_l of ≈ 56 km (Fig. 3c), much larger than the ≈ 13 km indicated by the LAB model (Fig. 2). Further, at constant ρ_l, we would predict the absence of a mantle lithosphere throughout large parts of the domain. The amplitude of l_l RMS variations depends on f_2, and fluctuations of ~60 km are more typical for thickness estimates from tomography than for L from LAB depth. As we show below, however, these trade-offs do not seem to reduce δt_l estimates, implying that the origin of the residual topography as shown in Fig. 3 may lie in mantle flow or crustal density variations. Specifically, there are a number of pronounced negative residual topography anomalies along the Sierra Nevada and Cascades, raising the question of whether these (or other) anomalies are due to relatively high crustal density anomalies, or perhaps are being pulled down by ongoing subduction, or lithospheric delamination (e.g., Xue and Allen, 2007; James et al., 2011; Schmandt and Humphreys, 2011; Gilbert et al., 2012; Karlstrom et al., 2012).

Fig. 5a shows the inferred crustal density anomaly if all residual topography in Fig. 3b were caused by crustal density variations at constant lithospheric thickness (Eq. (4)). To assess the degree to which these density variations may be reflected in other data, we compare with crustal density anomalies derived independently by Lowry and Pérez-Gussinyé (2011) based on v_P/v_S ratios from receiver functions and gravity constraints (Fig. 5b). The RMS of the density model derived from seismic velocities (~24 kg/m^3) is much smaller than would be needed for perfect isostasy (≈ 49 kg/m^3), but the overall patterns agree moderately well ($r \sim 0.6$). The crust within coastal orogens and parts of the Colorado Plateau is predicted to be denser than average, and the central Basin and Range may be lighter. If we use the crustal density variations from LPG (Fig. 5b) for the isostatic balance, we obtain the residual topography shown in Fig. 5c. Correlation analysis shows that this model explains ~65% of the topography, and patterns are consistently better predicted than for the constant density model for all wavelengths ≥750 km (Fig. 4e).
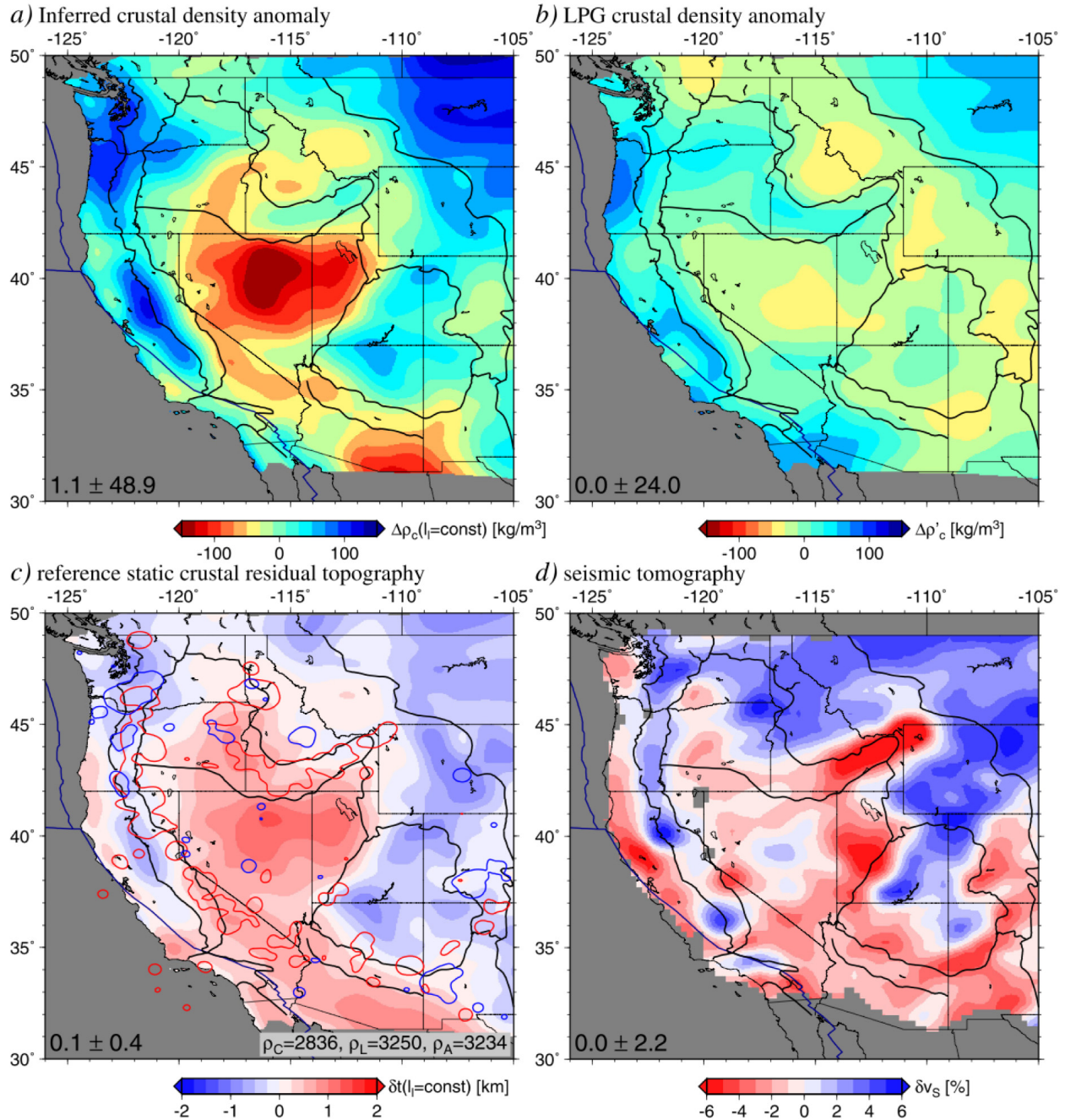
Fig. 5. (a) Crustal density anomaly associating all residual topography of Fig. 3c with $\Delta\rho_c$ (Eq. (4)). (b) Crustal density anomaly input model from LPG based on v_P/v_S ratios (Lowry and Pérez-Gussinyé, 2011). (c) Residual topography, δt_c, as in Fig. 3b, but allowing for density anomalies as in (b). Contours are regions with large clusters of Cenozoic volcanic samples with ages ≤20 Ma (red) or >20 Ma (blue) as of the earthchem.org database as of 05/2012 (cf. McQuarrie and Oskin, 2010, and note that this does not capture all recent volcanism). (d) Seismic shear wave tomography anomaly averaged from 90 to 160 km depth from the well-defined model regions of Schmandt and Humphreys (2010) (regional mean, $\approx$ –0.9% removed).

The remaining anomalies of Fig. 5c are then inferred to be either due to lithospheric density variations ("static"), or due to ongoing, dynamic support due to present-day

mantle flow. Both mechanisms should have a signature in seismic tomography models with good shallow resolution. We computed the correlation of the residual topography, δt_c, signal of Fig. 5c with seismic velocity anomalies, δv_S, at different layers and found a consistent minimum at ~100 km depth for the models discussed in Becker (2012). Fig. 5d displays a lithospheric depth (90–160 km) averaged slice of the SH11-TX model (Schmandt and Humphreys, 2010) (anti-correlation of δv_S with δt_c at 100 km depth is $r \approx$ –0.5), as an example. Results for DNA10 (Obrebski et al., 2011) are similar, at $r \approx$ –0.7, for example.

If we allow for lithospheric density variations at constant lithospheric thickness, we can reduce the RMS of the anomalous topography slightly compared to Fig. 5c. For this experiment, we first infer $\Delta\rho_l$ by scaling the tomographic structure of Fig. 5d by $d\ln\rho_l/d\ln v_S$ = 0.2. Such a scaling is, of course, a crude simplification, because compositional effects or partial melt will perturb density and velocity differently than thermal effects (e.g., Goes and van der Lee, 2002; Stixrude and Lithgow-Bertelloni, 2010). Given the $\approx$ 2% RMS variations in $d\ln v_S$, we obtain a $\Delta\rho_l$ RMS of ~14 kg/m^3 (equivalent to ~155 m at $\bar{l}_l$ = 36 km, Eq. (5), compared to $\approx$ 26 kg/m^3, or 325 m, Eq. (4), for the crustal density anomalies of Fig. 5b).

For this test, we allow for an arbitrarily thickened mantle lithosphere at $\bar{l}_l$ = 72 km, i.e. twice the LAB P-RF estimate (Fig. 2a), to give larger weight to the f_2 term in Eq. (1). LAB studies from receiver functions might provide an underestimate of mantle lithospheric thickness. However, we do not think that $\bar{l}_l$ = 72 km is realistic but the actual mean thickness of ~40 km seems more plausible. Correspondingly, we only discuss these end-member examples in order to provide a conservative estimate of how much of the topography might be explained without having to invoke a deep mantle source. This "static" correction due to lithospheric density variations from tomography leads to a moderate adjustment of residual topography (Fig. 6a), at slightly improved correlations compared to the reference crustal residual model of Fig. 5c (cf. Fig. 4e and f). Were we to use the actual LM P-RF LAB estimate of $\bar{l}_l$ = 36 km, patterns are similar to those shown in Fig. 6a, albeit at increased estimates of ρ_a. Combining variable ρ_l with the lithospheric thickness variations from LM does not notably modify residuals further.

Residual topography for a second $\Delta\rho_l$ test is shown in Fig. 6b. Here, lithospheric density anomalies are based on the thermal mass anomaly of LPG who used heat flow measurements to estimate lateral variations in isotherms and corresponding density variations (RMS ~8 kg/m^3; cf. Lowry and Pérez-Gussinyé, 2011). While local features, such as the Snake River Plain, are modified for this model, overall patterns are very similar to those of the reference model (Fig. 5c), and the topography correlation and power (Fig. 4g) is also similar to the other $\Delta\rho_l$ model of Fig. 6a.

It is clear that compositional variations within the lithosphere may affect the density structure (Jordan, 1978), and assuming a linear scaling between seismic velocity and density anomalies as in Fig. 6a may overemphasize "hot" anomalies. Moreover, tomographic model amplitudes, as opposed to patterns, are quite uncertain given the intricacies of regularized inversions (e.g. Becker, 2012). The thermal anomaly estimate of Fig. 6b has its own uncertainties, but it is an independent estimate of lithospheric

heterogeneity. Given that both tests consistently show relatively small differences between Fig. 5 and Fig. 6, anomalies within the lithosphere itself are, however, likely not the cause of the majority of the residual topography signal.
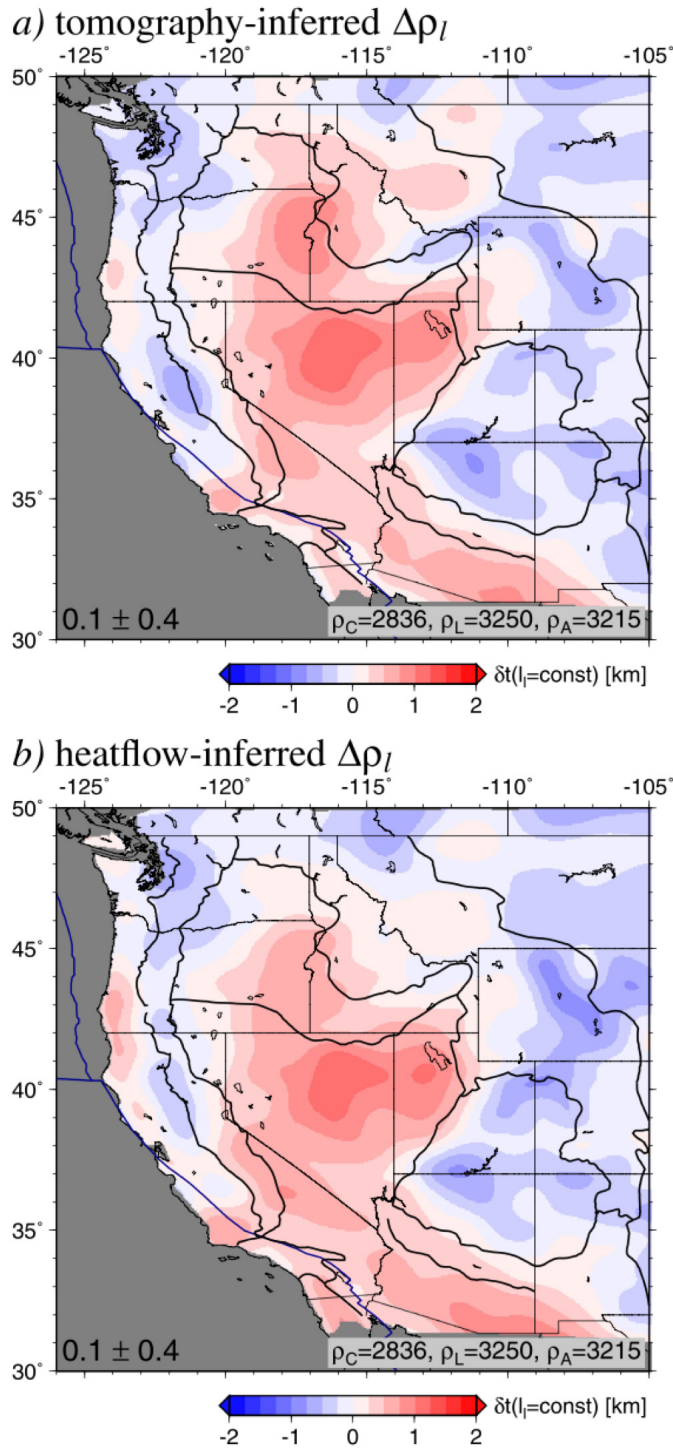

a) tomography-inferred $\Delta\rho_l$

b) heatflow-inferred $\Delta\rho_l$

Fig. 6. Residual topography for the LPG crustal model as in Fig. 5c, but allowing for lithospheric density variations, $\Delta\rho_l$. (a) as inferred from the seismic tomography average in Fig. 5d, using a uniform scaling of $d\ln\rho_l / d\ln v_S = 0.2$ at ρ_l =3250 kg/m^3, and a lithospheric mantle thickness of $\bar{l}_l =$ 72 km, doubled from the LAB P-RF estimate of Fig. 2 for testing purposes. (b) Using the mass anomaly from Lowry and Pérez-Gussinyé's (2011) heat flow estimate of thermal boundary layer structure.

Given these vagaries of lithospheric density anomalies, and the observation that the Moho model from Lowry and Pérez-Gussinyé (2011) leads to the superior correlations with topography (Fig. 4), we take the most highly correlated model without arbitrary assumptions about lithospheric contributions, as in Fig. 5c, as a reference. For such models, ≥60% of the topography variations within the whole domain can be attributed to isostatic balance of a heterogeneous crust. Correlation between isostatic expectations and actual topography on its own does, of course, not provide a measure to decide between seismological models. Rather, it may guide the most conservative choice when proceeding to discuss the residual topography anomalies in terms of possible dynamic causes.

It thus appears from Fig. 3, Fig. 4, Fig. 5 and Fig. 6 that the broad, anomalously high topography of the Basin and Range may indeed be supported by upwellings associated with upper mantle anomalies (Parsons et al., 1994; Lowry et al., 2000). Likewise, the downward pull due to active subduction beneath the Cascade arc, as imaged by tomography, may be associated with negative dynamic

topography there. The overlain contours of Cenozoic volcanism from the earthchem.org database (cf. McQuarrie and Oskin, 2010) in Fig. 5c show that most activity outside past or presently active subduction regions is found at edges of high or low dynamic topography (cf. Roy et al., 2009; Reid et al., 2012), and this might suggest a link between volcanism and upwellings, perhaps modulated by slab dynamics (e.g., Xue and Allen, 2007; Faccenna et al., 2010). Yellowstone itself and the Snake River plain are, on the other hand, seismically very slow, yet do not show a pronounced residual topography. This indicates that factors other than temperature such as partial melt or composition affect velocity anomalies more strongly in these regions.

3.2. Comparison of residual topography with mantle flow based estimates

We first explore the role of different mantle tomography inputs within flow model predictions using the Hager and O'Connell (1981) approach without any lateral viscosity variations, implying a poor match of surface velocities (Ricard and Vigny, 1989). Fig. 7a shows our model estimates of surface deflections, δz_{dyn}, (the "dynamic" component of topography) using the global tomography model TX2008 (Simmons et al., 2007). A modified version of this model was used by Moucha et al. (2008; 2009) after optimizing the match between flow models and geophysical observations by allowing for compositional anomalies within the mantle. Moucha et al. (2008) further suggest that the long-wavelength structure with degree $\ell \leq 12$, such as the tilting of North America apparent in Fig. 7a, should be removed from the δz_{dyn} predictions; we follow this processing step in Fig. 7b.

Both of our dynamic topography estimates for TX2008 are qualitatively similar to those of Moucha et al. (2008), implying that compositional anomalies, which are absent in our models, different surface motions, and other modeling choices are not affecting the predictions qualitatively. In particular, the filtered result of Fig. 7b shows a focused dynamic topography high centered on the Colorado Plateau. If we compute δz_{dyn} using the global S40RTS model (Ritsema et al., 2011) (Figs. 7c and d), large wavelength patterns are similar. However, the short wavelength filtered version is different. Such sensitivity is expected, given that global tomography models agree well with each other only at the largest wavelengths of $\ell \leq 15$ (Becker and Boschi, 2002). This means that global tomography models should be employed cautiously when analyzing features on scales of ≤ 2000 km, and regional(ly augmented) tomographic models are perhaps preferred for such applications.

Figs. 7e and f show mantle-flow induced topography when the regional SH11-TX tomography (Schmandt and Humphreys, 2010) is embedded in TX2008. Such merging of models is not straightforward and can lead to edge effects, making predictions in Fig. 7e within oceanic plates not necessarily reliable. However, for our discussion of the western U.S. tectonics, δz_{dyn} will mainly depend directly on structure imaged by SH11-TX, and edge effects are less important. Using the improved structural information provided by the regional data that went into SH11-TX, the dynamic topography predictions are very different from those of the global models, regardless of whether long-wavelength structure is filtered out or not. In particular, it is mainly the regions surrounding the Colorado Plateau that are predicted to be pushed up by mantle flow, along with some negative dynamic topography due to subduction (cf. Fig. 5d).
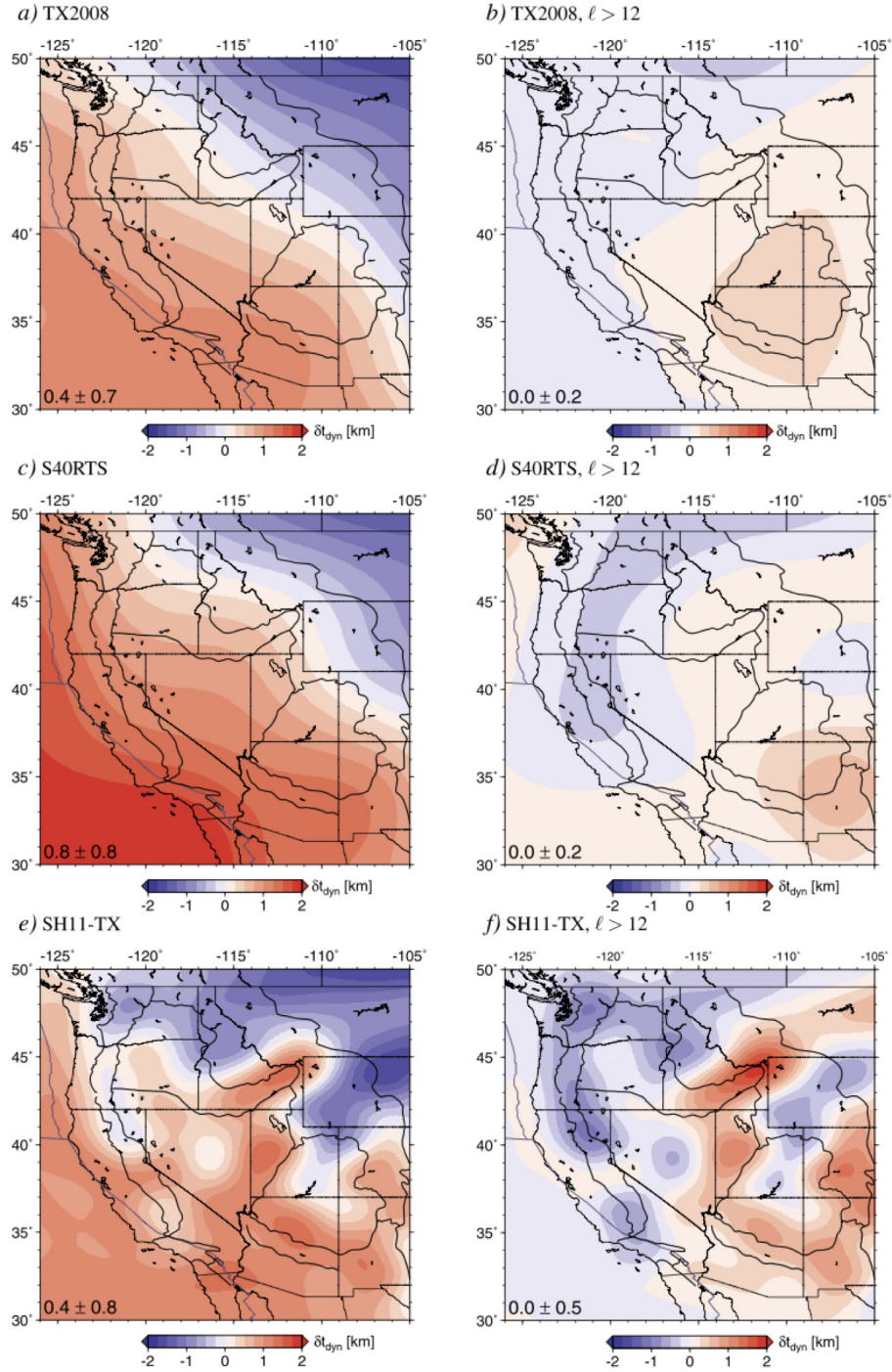
Fig. 7. Dynamic topography from present-day mantle convection, δz_{dyn}, estimated using a spectral, Hager and O °Connell (1981) type circulation model (Becker et al., 2013) with free slip surface boundary conditions and only radial viscosity variations. All tomographic velocity anomalies deeper than 100 km are scaled to density as $d \ln \rho_l / d \ln v_S = 0.18$. Left plots (a, c, e) show full predictions, right ones (b, d, f) only short-wavelength filtered estimates, setting all contributions of spherical harmonic degree $\ell \le 12$ to zero (cf. Moucha et al., 2008). (a) and (b) use global TX2008 tomography (Simmons et al., 2007); (c) and (d) global S40RTS (Ritsema et al., 2011); and (e) and (f) the regional SH11-TX model (Schmandt and Humphreys, 2010) (cf. Fig. 5d), embedded in TX2008.

Predictions of mantle flow topography for other regional models such as DNA10 (Obrebski et al., 2011) are similar ($r = 0.92$ and $r = 0.75$ for Fig. 7e and f, respectively), as expected (Becker, 2012). We can compare the dynamic surface deflections from instantaneous mantle flow (derived from SH11-TX as in Fig. 7e) with the residual topography estimates after removing the reference static model of Fig. 5c. For those models, correlations are $r = 0.55$ if we convert all layers of tomographic anomalies to density to drive flow, and $r = 0.53$ if all anomalies shallower than 200 km are set to zero. This indicates that, while shallow mantle structure dominates estimates of viscous tractions at the surface, our overall conclusions are insensitive to the choice of depth cutoff.

To test the sensitivity to second-order lithospheric and mantle effects, Fig. 8 shows surface deflection due to mantle flow from three different finite element computations that incorporate some plate tectonic complexities. Fig. 8a follows a dynamically consistent flow modeling approach, allowing for free relative plate motions at prescribed weak zones, following Becker and Faccenna (2011). The model has only radial viscosity variations, apart from the reduced viscosity weak zones within the lithosphere, and is driven by the SH11-TX model as in Fig. 7e. Given the numerical resolution, some of the detailed features of the structural model result in more pronounced local features, but general results for δz_{dyn} compare well with the spherical harmonic estimate of Fig. 7e. The model of Fig. 8a differs in terms of the detailed implementation; a major qualitative difference are surface velocities, which are now more plate-like, though certainly not alike observed crustal motions (cf. Forte et al., 2010 and Ghosh et al., 2013). The dynamic topography estimates are, however, similar at the $r = 0.94$ level.
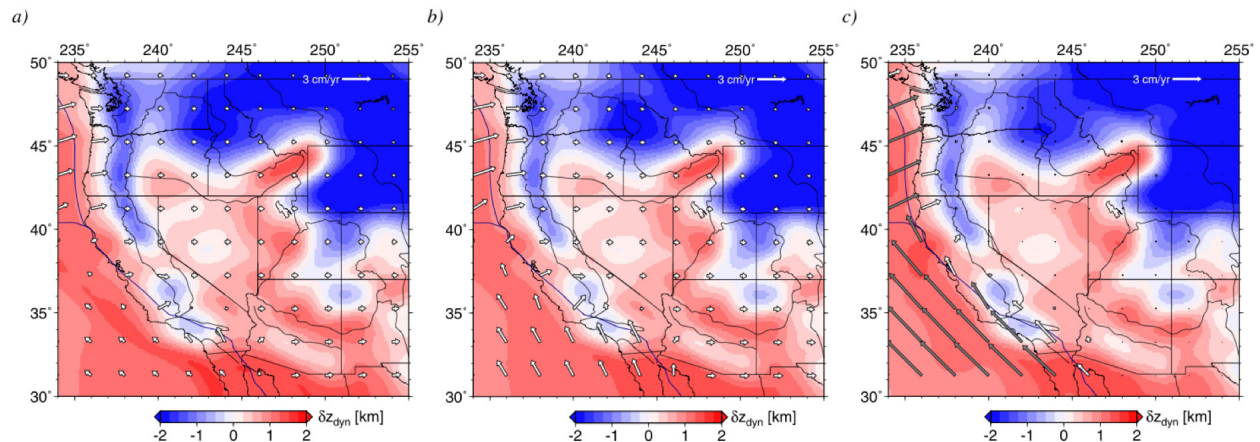

Fig. 8. Dynamic topography from mantle flow and surface velocities (vectors, North America fixed frame) for different mechanical boundary conditions and viscosity models. Mantle density is inferred from the embedded SH11-TX tomography of Schmandt and Humphreys (2010) as in Fig. 7c. (a) Free-slip mantle computation with prescribed weak zones and only radial viscosity variations, with all parameters but density anomalies as in Becker and Faccenna (2011). (b) Like (a), but including lateral viscosity variations as given by a variable thickness lithosphere model, inferred from LM-P (Fig. 2) underneath continental regions. (c) Only radial viscosity variations, but prescribed surface motions within the Pacific plate (gray vectors), and North American domain free to move (white vectors; cf. Faccenna and Becker, 2010).

Fig. 8b indicates how surface velocities and δz_{dyn} are affected by lateral viscosity variations due a lithospheric thickness model which applies a half-space cooling type of

structure within the oceanic plates, and follows the P-RF LAB depth of Levander and Miller (2012) as in Fig. 2. The regions above the inferred LAB depth are set to $150\eta_0$, with all upper-mantle regions set to the reference viscosity, η_0. Surface velocities for the Pacific plate are increased given the relatively thin lithosphere (hence relatively low viscosity asthenosphere at ~100 km depth), but dynamic topography is, again, barely affected (cf. Moucha et al., 2007; Ghosh et al., 2010). Lastly, Fig. 8c follows the approach of Faccenna and Becker (2010) and has the Pacific plate motions prescribed and leaves North America free to move. Again, dynamic topography patterns are insensitive to such changes in surface kinematics, even in their details. More spatially localized, or larger viscosity variation, models may affect dynamic topography patterns more strongly (Liu and Gurnis, 2010), but we expect the general features for the western U.S. to be relatively stable.

4. Discussion

We suggest that models with crustal density anomalies as inferred from v_P/v_S analysis (Lowry and Pérez-Gussinyé, 2011) improve upon the purely Moho and LAB depth-based isostatic topography estimates, and we use the resulting model of Fig. 5c as a reference for residual topography. The substantial contribution of crustal density variations to isostasy, i.e. a mix between Pratt and Airy end-members, is consistent with the findings from regional studies, such as Coblentz et al. (2011).

One might argue, however, that because v_P/v_S variations in Lowry and Pérez-Gussinyé's (2011) model are partly constrained by gravity, mass anomalies from asthenospheric depths may contaminate their estimate of crustal density, and hence make the match between isostatically required and "observed" density anomalies somewhat circular. Fig. 4h shows the correlation of the LPG Bouguer gravity model to observed gravity. Coherence is lowest at wavelengths <200 km that are aliased by seismic sampling, but even at longer wavelengths, the correlation is imperfect (r^2 ~ 0.8). This is consistent with Lowry and Pérez-Gussinyé's interpretation that significant residual gravity remains at long wavelengths that cannot be accommodated by the crustal seismic model. The correlation is similarly imperfect at long wavelengths when comparing gravity derived from their crustal model to observed topography. Comparison to the coherence between observed gravity and topography lends further confidence that the lower coherence at long wavelengths in the other two curves is related to real mass variations that are not reflected in the LPG crustal model.

Even if one suspects that deeper mass variations may contaminate LPG's crustal estimates, our reference model minimizes the topographic residual, and thus represents the most conservative choice when discussing the residuals in terms of possible mantle processes. Comparing our reference estimate of residual topography of Fig. 5c and the surface deflection from mantle flow as in Fig. 7 and Fig. 8, it is apparent that several of the anomalous topographic features may be due to mantle flow. The correlation between these two independently derived fields is r ~ 0.6 for most model combinations.

Several features emerge from our analysis. Firstly, the dynamic depression of topography along the Cascadia arc appears to respond to slabs imaged by tomography in regions of active subduction. It is intriguing that this topographic depression may extend even further to the south, where subduction ceased in the Middle Miocene. This

suggests that active flow is maintaining a surface depression of several hundreds of meters, more than 10–15 Myrs after the break-off of the slab (cf. Schmandt and Humphreys, 2011; Pikser et al., 2012). This scenario could be useful to test models of topographic response to slab tearing.

Secondly, the absence of large topographic anomalies in the Colorado Plateau as seen in the residual topography estimate is corroborated by the flow computations. In addition, residual topography and mantle flow models agree in delineating a positive signal on the western edge of the plateau. While our modeling only concerns present-day or very recent (≤1 Ma) tectonics, this model supports the hypothesis that most of the uplift of the core of the Colorado Plateau occurred earlier in the geological history (e.g., Liu and Gurnis, 2010; Flowers, 2010), and the region may now be considered stable. Our model also supports the suggestion that the areas surrounding the edges of the plateau, at least to the west and south, are dynamically supported by shallow, upper mantle convection (Roy et al., 2009; van Wijk et al., 2010; Levander et al., 2011; Karlstrom et al., 2012).

Thirdly, regions of disagreement between residual topography from crustal structure and surface deflection from mantle flow include the central Basin and Range, which is inferred to have the strongest positive residual topography but has a local minimum in topography from mantle flow. Indeed, for the central Basin and Range region, evidence from uplift, crustal extension, and volcanism support that at least in the Lower Miocene-Oligocene (McQuarrie and Oskin, 2010) this region was dynamically uplifted (Parsons et al., 1994). A possible explanation for this mismatch between residual and dynamic topography may be a trade-off between isotropic and anisotropic structure in seismological models in the presence of laterally-variable radial anisotropy (e.g. Savage and Sheehan, 2000), or the signature of mantle depletion.

As expected from maps of shallow tomography layers (Fig. 5d), the Snake River plain is predicted to have high topography but is at the background level in the residual topography estimate. A more detailed exploration of the crustal and uppermost mantle structure and the effects of melting, as well as lithospheric modification, on the velocity and density signature of such anomalies should be capable of turning the background models provided by this study into more detailed process-level models for upper mantle, thermo-chemical, small scale convection.

There was little improvement in terms of reduction of residual topography for "static" models when variations of the mantle lithospheric thickness as inferred from receiver function LAB estimates were included. This implies that the transitional region imaged by seismic methods may, to first order, not correspond to an effective thickness of an anomalously dense lithosphere, even in the western U.S. where the compositional complexities of cratonic lithosphere may be less of an issue (e.g. Jordan, 1978 and Lee et al., 2005). Instead, the LAB may be detecting a transition in volatile state, perhaps leading to focusing of anisotropy below the strong lithosphere in the relatively weaker, volatile rich asthenosphere. The LAB may be more sensitive to lithospheric strength rather than thermal or compositional thickness. However, the complexities of LAB structure (e.g., Rychert and Shearer, 2009; Yuan and Romanowicz, 2010; Kumar et al.,

2012; Levander and Miller, 2012) require a more detailed analysis of the trade-off between composition and temperature for an isostatic balance.

5. Conclusions

Making use of structural seismology information on lithospheric and mantle heterogeneity, we show that passive USArray imaging allows for an improved analysis of the origin of western U.S. topography and tectonics. Roughly 70% of the non-flexural topography can be explained by isostasy of a variable thickness crust, if lateral variations in crustal density as informed by seismology are included. However, employing seismically determined lithospheric thickness, or lithospheric density, variations does not lead to improved isostatic models. This suggests the dominance of large uncertainties due to compositional heterogeneity, that the LAB may predominantly sense mechanical rather than buoyancy effects, that the relationship between the LAB and lithospheric thickness may be locally too complex to be captured by a large-scale isostatic balancing approach, or a combination of all three.

The remaining non-isostatic, "dynamic" component of topography due to present-day convective flow is prominent in the western United States. Most of the negative anomalies are likely due to subduction, such as the actively subducting Juan de Fuca plate and perhaps as remnants of formerly active convergence further to the south. Broad-scale positive residual topography in the Basin and Range and adjacent domains are substantiated, but we infer that the Colorado Plateau must have experienced most of its tectonically active uplift earlier in its history (≥1 Ma). Many of the persisting topography anomalies are consistent with predictions of surface deflections from mantle flow models, suggesting a present-day convective origin.

Acknowledgments

References

T. Atwater, Implications of plate tectonics for the Cenozoic tectonic evolution of western North America, Geol. Soc. Am. Bull., 81 (1970), pp. 3513–3536

I.W. Bailey, M.S. Miller, A. Levander, & K. Liu, v_S and density structure beneath the Colorado Plateau constrained by gravity anomalies and joint inversions of receiver function and phase velocity data, J. Geophys. Res., 117 (2012) http://dx.doi.org/10.1029/2011JB008522

C. Bassin, G. Laske, & G. Masters, The current limits of resolution for surface wave tomography in North America (abstract), Eos Trans. AGU, 81 (2000), p. F897

T.W. Becker, On recent seismic tomography for the western United States, Geochem. Geophys. Geosyst., 13 (2012), p. Q01W10 http://dx.doi.org/10.1029/2011GC003977

T.W. Becker, & L. Boschi, A comparison of tomographic and geodynamic mantle models, Geochem. Geophys. Geosyst., 3 (2002), p. 1 http://dx.doi.org/10.1029/2001GC000168

T.W. Becker, & C. Faccenna, Mantle conveyor beneath the Tethyan collisional belt, Earth Planet. Sci. Lett., 310 (2011), pp. 453–461

T.W. Becker, B. Steinberger, & C. O'Neill, HC – A global mantle circulation solver following Hager and O'Connell (1981) and Steinberger (2000), Available online at http://geodynamics.usc.edu/~becker/sdata.html (2013) Accessed 01/2013

P. Bird, Continental delamination and the Colorado Plateau, J. Geophys. Res., 84 (1979), pp. 7561–7571

P. Bird, An updated digital model of plate boundaries, Geochem. Geophys. Geosyst., 4 (3) (2003), p. 1027 http://dx.doi.org/10.1029/2001GC000252

J. Braun, The many surface expressions of mantle dynamics, Nat. Geosci., 3 (2010), pp. 825–833

R.L. Carlson, & H.P. Johnson, On modeling the thermal evolution of the oceanic upper-mantle – an assessment of the cooling plate model, J. Geophys. Res., 99 (1994), pp. 3201–3214

C.G. Chase, J.A. Libarkin, & A.J. Sussman, Colorado Plateau: Geoid and means of isostatic support, Int. Geol. Rev., 44 (2002), pp. 575–587

D. Coblentz, C.G. Chase, K.E. Karlstrom, & J. van Wijk, Topography, the geoid, and compensation mechanisms for the southern Rocky Mountains, Geochem. Geophys. Geosyst., 12 (2011), p. Q04002 http://dx.doi.org/10.1029/2010GC003459

H.P. Crotwell, & T.J. Owens, Automated receiver function processing, Seismol. Res. Lett., 76 (2005), pp. 702–709 Data available online at http://www.iris.washington.edu/ears Accessed 01/2013

S.T. Crough, & G.A. Thompson, Thermal model of continental lithosphere, J. Geophys. Res., 81 (1976), pp. 4857–4862

S.T. Crough, & G.A. Thompson, Upper mantle origin of Sierra Nevada uplift, Geology, 5 (1977), pp. 396–399

R. Crow, K. Karlstrom, Y. Asmerom, B. Schmandt, V. Polyak, & S.A. DuFrane, Shrinking of the Colorado Plateau via lithospheric mantle erosion: Evidence from Nd and Sr isotopes and geochronology of Neogene basalts, Geology, 39 (2010), pp. 27–30

D. Eaton, F. Darbyshire, H. Evans, R.L. Grütter, A.G. Jones, & X. Yuan, The elusive lithosphere–asthenosphere boundary (LAB) beneath cratons, Lithos, 109 (2009), pp. 1–22

C. Faccenna, & T.W. Becker, Shaping mobile belts by small-scale convection, Nature, 465 (2010), pp. 602–605

C. Faccenna, T.W. Becker, S. Lallemand, Y. Lagabrielle, F. Funiciello, & C. Piromallo, Subduction-triggered magmatic pulses. A new class of plumes? Earth Planet. Sci. Lett., 209 (2010), pp. 54–68

K.M. Fischer, D.L. Ford, H.A. Abt, & C.A. Rychert, The lithosphere–asthenosphere boundary, Annu. Rev. Earth Planet. Sci., 38 (2010), pp. 551–575

N. Flament, M. Gurnis, & R.D. Müller, A review of observations and models of dynamic topography, Lithosphere, 5 (2013), pp. 189–210

R.M. Flowers, The enigmatic rise of the Colorado Plateau, Geology, 38 (2010), pp. 671–672

A.M. Forte, R. Moucha, N. Simmons, S. Grand, & J. Mitrovica, Deep-mantle contributions to the surface dynamics of the North American continent, Tectonophysics, 481 (2010), pp. 3–15

A. Frassetto, H. Gilbert, G. Zandt, S. Beck, & M.J. Fouch, Support of high topography in the southern Basin and Range based on composition and architecture of the crust in the Basin and Range and Colorado Plateau, Earth Planet. Sci. Lett., 243 (2006), pp. 62–73

A. Ghosh, T.W. Becker, & E.D. Humphreys, Dynamics of the North American continent, Geophys. J. Int., 194 (2013), pp. 651–669

A. Ghosh, T.W. Becker, & S. Zhong, Effects of lateral viscosity variations on the geoid, Geophys. Res. Lett., 37 (2010), p. L01301 http://dx.doi.org/10.1029/2009GL040426

H. Gilbert, Y. Yang, D.W. Forsyth, C.H. Jones, T.J. Owens, G. Zandt, & J. Stachnik, Imaging lithospheric foundering in the structure of the Sierra Nevada, Geosphere, 8 (2012), pp. 1300–1310

S. Goes, & S. van der Lee, Thermal structure of the North American uppermost mantle inferred from seismic tomography, J. Geophys. Res., 107 (2002), p. 2050 http://dx.doi.org/10.1029/2000JB000049

M. Gurnis, J.X. Mitrovica, J. Ritsema, & H.-J. van Heijst, Constraining mantle density structure using geological evidence of surface uplift rates: The case of the African superplume, Geochem. Geophys. Geosyst., 1 (2000), p. 1020 http://dx.doi.org/10.1029/1999GC000035

B.H. Hager, & R.J. O'Connell, A simple global model of plate dynamics and mantle convection, J. Geophys. Res., 86 (1981), pp. 4843–4867

E.D. Humphreys, & D. Coblentz, North American dynamics and western U.S. tectonics, Rev. Geophys., 45 (2007), p. RG3001 http://dx.doi.org/10.1029/2005RG000181

R.D. Hyndman, & C.A. Currie, Why is the North America Cordillera high? Hot backarcs, thermal isostasy, and mountain belts, Geology, 39 (2011), pp. 783–786

D.E. James, M.J. Fouch, R.W. Carlson, & J.B. Roth, Slab fragmentation, edge flow and the origin of the Yellowstone hotspot track, Earth Planet. Sci. Lett., 311 (2011), pp. 124–135

C.H. Jones, J.R. Unruh, & L. Sonder, The role of gravitational potential energy in active deformation in the southwestern United States, Nature, 381 (1996), pp. 37–41

C.H. Jones, B.P. Wernicke, G.L. Farmer, J.D. Walker, D.S. Coleman, L.W. McKenna, & F.V. Perry, Variations across and along a major continental rift: an interdisciplinary study of the Basin and Range Province, western USA, Tectonophysics, 213 (1992), pp. 57–96

T.H. Jordan, Composition and development of the continental tectosphere, Nature, 274 (1978), pp. 544–548

S.-I. Karato, Importance of anelasticity in the interpretation of seismic tomography, Geophys. Res. Lett., 20 (1993), pp. 1623–1626

K.E. Karlstrom, D. Coblentz, K. Dueker, W. Ouimet, E. Kirby, J.V. Wijk, B. Schmandt, S. Kelley, G. Lazear, L. Crossey, R. Crow, A. Aslan, A. Darling, R. Aster, J. MacCarthy, S. Hansen, J. Stachnik, D. Stockli, R. Garcia, M. Hoffman, R. McKeon, J. Feldman, M. Heizler, M. Donahue, & the CREST Working Group, Mantle-driven dynamic uplift of the Rocky Mountains and Colorado Plateau and its surface response: Toward a unified hypothesis, Lithosphere, 4 (2012), pp. 3–22

P. Kumar, R. Kind, X. Yuan, & J. Mechie, USArray receiver function images of the lithosphere–asthenosphere boundary, Seismol. Res. Lett., 83 (2012), pp. 486–491

A.H. Lachenbruch, & P. Morgan, Continental extension, magmatism and elevation; formal relations and rules of thumb, Tectonophysics, 174 (1990), pp. 39–62

Y. Le Stunff, & Y. Ricard, Topography and geoid due to lithospheric mass anomalies, Geophys. J. Int., 133 (1995), pp. 982–990

C.-T.A. Lee, A. Lenardic, C.M. Cooper, F. Niu, & A. Levander, The role of chemical boundary layers in regulating the thickness of continental and oceanic thermal boundary layers, Earth Planet. Sci. Lett., 230 (2005), pp. 379–395

A. Levander, & M.S. Miller, Evolutionary aspects of the lithosphere discontinuity structure in the western U.S., Geochem. Geophys. Geosyst., 13 (2012), p. Q0AK07 http://dx.doi.org/10.1029/2012GC004056

A. Levander, B. Schmandt, M.S. Miller, K. Liu, K.E. Karlstrom, R.S. Crow, C.-T. Lee, & E.D. Humphreys, Regional Colorado Plateau uplift by delamination and thermo-chemical downwelling of North American lithosphere, Nature, 472 (2011), pp. 461–465

L. Liu, & M. Gurnis, Dynamic subsidence and uplift of the Colorado Plateau, Geology, 38 (2010), pp. 663–666

A.R. Lowry, & M. Pérez-Gussinyé, The role of crustal quartz in controlling Cordilleran deformation, Nature, 471 (2011), pp. 353–357

A.R. Lowry, N.M. Ribe, & R.B. Smith, Dynamic elevation of the Cordillera, western United States, J. Geophys. Res., 105 (2000), pp. 23371–23390

N. McQuarrie, & M. Oskin, Palinspastic restoration of NAVDat and implications for the origin of magmatism in southwestern North America, J. Geophys. Res., 115 (2010), p. B10401 http://dx.doi.org/10.1029/2009JB006435

N. McQuarrie, & D.W. Rodgers, Subsidence of a volcanic basin by flexure and lower crustal flow: The eastern Snake River Plain, Tectonics, 17 (1998), pp. 203–220

K. Milner, T.W. Becker, L. Boschi, J. Sain, D. Schorlemmer, & H. Waterhouse, The Solid Earth Research and Teaching Environment: a new software framework to share research tools in the classroom and across disciplines, Eos Trans. AGU, 90 (12) (2009), p. 104

W.D. Mooney, G. Laske, & G. Masters, CRUST 5.1: a global crustal model at 5°×5°, J. Geophys. Res., 103 (1998), pp. 727–747

R. Moucha, A.M. Forte, J.X. Mitrovica, & A. Daradich, Lateral variations in mantle rheology: implications for convection related surface observables and inferred viscosity models, Geophys. J. Int., 169 (2007), pp. 113–135

R. Moucha, A.M. Forte, D.B. Rowley, J.X. Mitrovica, N.A. Simmons, & S.P. Grand, Mantle convection and the recent evolution of the Colorado Plateau and the Rio Grande Rift valley, Geology, 36 (2008), pp. 439–442

R. Moucha, A.M. Forte, D.B. Rowley, J.X. Mitrovica, N.A. Simmons, & S.P. Grand, Deep mantle forces and the uplift of the Colorado Plateau, Geophys. Res. Lett., 36 (2009), p. L19310 http://dx.doi.org/10.1029/2009GL039778

NOAA, 2006. 2-minute Gridded Global Relief Data (ETOPO2v2). U.S. Department of Commerce, National Oceanic and Atmospheric Administration, National Geophysical Data Center, Boulder, Colorado, http://www.ngdc.noaa.gov/mgg/fliers/06mgg01.html, Accessed 01/2013.

M. Obrebski, R.M. Allen, F. Pollitz, & S.-H. Hung, Lithosphere–asthenosphere interaction beneath the western United States from the joint inversion of body-wave traveltimes and surface-wave phase velocities, Geophys. J. Int., 185 (2011), pp. 1003–1021

S.V. Panasyuk, & B.H. Hager, Models of isostatic and dynamic topography, geoid anomalies, and their uncertainties, J. Geophys. Res., 105 (2000), pp. 28,199–28,209

T. Parsons, & J. McCarthy, The active southwest margin of the Colorado Plateau: Uplift of mantle origin, Geology, 107 (1995), pp. 139–147

T. Parsons, G.A. Thompson, & N.H. Sleep, Mantle plume influence on the Neogene uplift and extension of the U.S. western Cordillera, Geology, 22 (1994), pp. 83–86

G.L. Pavlis, K. Sigloch, S. Burdick, M.J. Fouch, & F. Vernon, Unraveling the geometry of the Farallon plate: Synthesis of three-dimensional imaging results from USArray, Tectonophysics, 532 (2012), pp. 82–102

J.E. Pikser, D.W. Forsyth, & G. Hirth, Along-strike translation of a fossil slab, Earth Planet. Sci. Lett., 331 (2012), pp. 315–321

M.R. Reid, R.A. Bouchet, J. Blichert-Toft, A. Levander, K. Liu, M.S. Miller, & F.C. Ramos, Melting under the Colorado Plateau, USA, Geology, 40 (2012), pp. 387–390

Y. Ricard, & C. Vigny, Mantle dynamics with induced plate tectonics, J. Geophys. Res., 94 (1989), pp. 17543–17559

J. Ritsema, H.J. van Heijst, A. Deuss, & J.H. Woodhouse, S40RTS: a degree-40 shear velocity model for the mantle from new Rayleigh wave dispersion, teleseismic traveltimes, and normal-mode splitting function measurements, Geophys. J. Int., 184 (2011), pp. 1223–1236

M. Roy, T.H. Jordan, & J. Pederson, Colorado Plateau magmatism and uplift by warming of heterogeneous lithosphere, Nature, 459 (2009), pp. 978–984

C.A. Rychert, & P.M. Shearer, A global view of the lithosphere–asthenosphere boundary, Science (2009), pp. 495–498

M.K. Savage, & A.F. Sheehan, Seismic anisotropy and mantle flow from the Great Basin to the Great Plains, western United States, J. Geophys. Res., 105 (2000), pp. 13715–13734

B. Schmandt, & E. Humphreys, Complex subduction and small-scale convection revealed by body-wave tomography of the western United States upper mantle, Earth Planet. Sci. Lett., 297 (2010), pp. 435–445

B. Schmandt, & E. Humphreys, Seismically imaged relict slab from the 55 Ma Siletzia accretion to the northwest United States, Geology, 39 (2011), pp. 175–178

V. Schulte-Pelkum, G. Biasi, A. Sheehan, & C. Jones, Differential motion between upper crust and lithospheric mantle in the central Basin and Range, Nat. Geosci., 4 (2011), pp. 619–623

W. Shen, M.H. Ritzwoller, & V. Schulte-Pelkum, A 3-D model of the crust and uppermost mantle beneath the Central and Western US by joint inversion of receiver functions and surface wave dispersion, J. Geophys. Res., 118 (2013), pp. 1–15 http://dx.doi.org/10.1029/2012JB009602

N.A. Simmons, A.M. Forte, & S.P. Grand, Thermochemical structure and dynamics of the African superplume, Geophys. Res. Lett., 34 (2007) http://dx.doi.org/10.1029/2006GL028009

J.E. Spencer, Uplift of the Colorado Plateau due to lithosphere attenuation during Laramide low-angle subduction, J. Geophys. Res., 101 (1996), pp. 13595–13609

B. Steinberger, Slabs in the lower mantle – results of dynamic modelling compared with tomographic images and the geoid, Phys. Earth Planet. Inter., 118 (2000), pp. 241–257

L. Stixrude, & C. Lithgow-Bertelloni, Thermodynamics of the Earth's mantle, Rev. Mineral. Geochem., 71 (2010), pp. 465–484

J.W. van Wijk, W.S. Baldridge, J. van Hunen, S. Goes, R. Aster, D. Coblentz, S.P. Grand, & J. Ni, Small-scale convection at the edge of the Colorado Plateau: Implications for topography, magmatism, and evolution of Proterozoic lithosphere, Geology, 38 (2010), pp. 611–614

P. Wessel, & W.H.F. Smith, New, improved version of the Generic Mapping Tools released, Eos Trans. AGU, 79 (1998), p. 579

M. Xue, & R.M. Allen, The Fate of the Juan de Fuca Plate: Implications for a Yellowstone plume head, Earth Planet. Sci. Lett., 264 (2007), pp. 266–276

H. Yuan, & B. Romanowicz, Lithospheric layering in the North American continent, Nature, 466 (2010), pp. 1063–1069

S. Zhong, M.T. Zuber, L. Moresi, & M. Gurnis, Role of temperature-dependent viscosity and surface plates in spherical shell models of mantle convection, J. Geophys. Res., 105 (2000), pp. 11063–11082